Global linear stability analysis of flow in a lined duct

L. Pascal[a,*], E. Piot[a], G. Casalis[a,b]

[a] *ONERA - The French Aerospace Lab, F-31055 Toulouse, FRANCE*
[b] *Institut Supérieur de l'Aéronautique et de l'Espace (ISAE-SUPAERO), Université de Toulouse, 10 avenue Édouard Belin - BP 54032 - 31055 Toulouse CEDEX 4, France*

Abstract

Eigenmodes of the linearised Euler equations are computed in order to study lined flow duct global stability. A simplified configuration is considered and the governing equations are discretised by means of the discontinuous Galerkin method. A biorthogonal technique is used to decompose the global eigenfunctions into local eigenmodes. The system dynamics switches from noise amplifier to resonator as the length of the liner is increased. The global mode in the liner region is shown to be mainly composed of a hydrodynamic unstable wave and a left-running acoustic mode.

Keywords: Acoustics, Global stability, Lined duct, Discontinuous Galerkin

1. Introduction

Acoustic lining is widely used to reduce sound. However, for specific liners and under particular flow conditions, some experiments have shown that a convective hydrodynamic instability may grow on the liner and is likely to lead to sound amplification [1, 2, 3, 4, 5, 6]. Evidence of such instabilities have been shown as well numerically [7, 8].

Hydrodynamic instabilities developing over an infinite acoustic lining have been extensively studied by means of local stability analysis. The first analyses have been made analytically under a constant mean flow assumption by taking into account the resulting vortex sheet on the lining through the Ingard-Myers boundary condition [9, 10]. Rienstra [11] showed the existence

*Corresponding author
Email address: lucas.pascal@onera.fr (L. Pascal)

of two hydrodynamic modes, one of them being potentially convectively unstable according to the so-called "Crighton-Leppington" criterion. However, Brambley [12] showed: firstly, that this criterion is flawed and that the Briggs-Bers criterion has to be used; and, secondly, that the Ingard-Myers boundary condition is mathematically ill-posed since it gives arbitrarily large exponential growth rates for arbitrarily small wavelengths and therefore precludes the Briggs-Bers stability analysis. Two well-posed boundary conditions have then been proposed by Rienstra and Darau [13] and Brambley [14] by considering a thin boundary layer on the acoustic lining. The boundary condition proposed by Brambley [14] was derived by following a more general approach [15] and was shown to give better results [16]. Brambley [17] showed that this boundary condition gives up to six surface modes, one of them potentially being a hydrodynamic convective instability.

Without the constant mean flow assumption, Rienstra and Vilenski [18] observed such a hydrodynamic instability by solving the problem numerically. Moreover, by considering a configuration representative of the experiments by Marx et al. [5], local stability analysis gives a hydrodynamic instability in agreement with the measurements [19, 20, 21]. Additionally, a recent study by Khamis and Brambley [22] found that viscosity may dramatically affect stability.

In real flow ducts, the liner is not infinite. Such configurations can be investigated analytically in a local approach by means of the Wiener-Hopf technique. Several studies (see for instance [23]) dealt with this problem but all of them considered mean flows with slipping boundary condition at the liner and used the Ingard-Myers boundary condition. As the problem is non-uniform, a natural alternative is to consider the global modal approach [24, 25], where the eigendirections are both the axial and normal directions. Such an approach is followed to characterise resonator dynamics [26] related to the presence of an absolutely unstable region. On the contrary, amplifier dynamics might be investigated by searching for the initial optimal perturbation (see for instance [27] and [28]) or the optimal harmonic forcing [29]. First attempts to account for the finite extent of the liner in modal and non-modal stability approaches have been presented by Pascal et al. [30] (in French) and Pascal et al. [31] respectively. More recently, Rahbari and Scalo [32] performed a global stability analysis of a fully-developed turbulent channel flow with porous wall. They found that the linearised Navier-Stokes equations support a globally unstable mode at a frequency close to the resonant frequency of the liner.

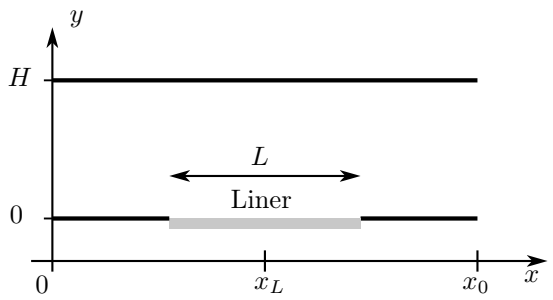

Figure 1: Geometry of the lined flow duct.

The present paper is intended to apply modal stability analysis to the configuration considered by Pascal et al. [31] in the time domain. This configuration was chosen as a simple toy model to study hydrodynamics instabilities developing in lined ducts. Moreover, the authors have reported [31, section 3] that this configuration might exhibit a stable or unstable resonator dynamics, depending on the length of the liner. Section 2 introduces the chosen configuration and the governing equations while their discretisation is presented in the following section. Sections 4 and 5 are devoted to the analysis of resonator dynamics by means of modal computations and biorthogonal decomposition.

2. Governing equations and chosen configuration

2.1. Linearised equations

The configuration studied in this paper is a partially lined two-dimensional flow duct of height H. The length of the liner is denoted by L. The geometry is depicted Fig. 1 together with the definition of the coordinates. x_L is the middle of the liner, x_0 the end of the physical domain. The main flow is purely in the axial direction (x-axis) and depends only on y.

The main flow (denoted with subscript 0) is assumed to be subsonic, stationary and homentropic. Moreover, the main density ρ_0 and the speed of sound a_0 are taken as constants [1]. The Mach number of the main flow is denoted M_0, the maximum and mean Mach numbers of mean velocity profile

[1]For a well-developed parabolic flow, taking a_0 as constant is not rigorously true but is a reasonable assumption.

are denoted respectively M and $\bar{M}$. Throughout the rest of this paper, the reference velocity, density, pressure, length and time are respectively $V_{ref} = a_0\bar{M}$, $\rho_{ref} = \rho_0$, $p_{ref} = \rho_{ref}V_{ref}^2$, $l_{ref} = H$ and $t_{ref} = l_{ref}/V_{ref}$.

We are interested by the evolution of a small perturbation, denoted $\boldsymbol{\varphi}$,superimposed to this mean flow. This perturbation is taken under the wave ansatz $\boldsymbol{\varphi}'(x,y,t) = \boldsymbol{\varphi}(x,y)e^{-\mathrm{i}\omega t}$ and is composed by the perturbation velocity vector $\boldsymbol{u} = u\boldsymbol{e_x} + v\boldsymbol{e_y}$ and by the perturbation pressure p: $\boldsymbol{\varphi} = (\boldsymbol{u}, p)$. The evolution of this perturbation is governed by the linearised Euler equations in the domain Ω, written under a matrix form as (the Einstein summation is used on x and y):

$$-\mathrm{i}\omega\boldsymbol{\varphi} + \boldsymbol{A_j}\partial_j\boldsymbol{\varphi} + \boldsymbol{B}\boldsymbol{\varphi} = 0 \tag{1}$$

where:

$$\boldsymbol{A_x} = \begin{pmatrix} M_0/\bar{M} & 0 & 1 \\ 0 & M_0/\bar{M} & 0 \\ 1 & 0 & M_0/\bar{M} \end{pmatrix}, \boldsymbol{A_y} = \begin{pmatrix} 0 & 0 & 0 \\ 0 & 0 & 1 \\ 0 & 1 & 0 \end{pmatrix}, \boldsymbol{B} = \begin{pmatrix} 0 & \partial_y\left(M_0/\bar{M}\right) & 0 \\ 0 & 0 & 0 \\ 0 & 0 & 0 \end{pmatrix}.$$

2.2. Boundary conditions

2.2.1. On the walls

At a wall (lined or not) an impedance boundary condition is imposed as defined by Eq. (2) where Z is the specific impedance and $\boldsymbol{n}$ is the outward-pointing unit normal vector.

$$p = Z\boldsymbol{u}\cdot\boldsymbol{n} \tag{2}$$

In order to avoid singular behaviour when $Z = 0$ (soft wall) or $Z \to \infty$ (hard wall), the coefficient $\beta = (Z-1)/(Z+1)$ is introduced. The boundary condition Eq. (2) becomes:

$$(\beta - 1)p + (\beta + 1)\boldsymbol{u}\cdot\boldsymbol{n} = 0\ . \tag{3}$$

Finally, no-slip boundary condition is imposed on the main flow, which justifies the choice of Eq. (3) rather than a (enhanced) Myers boundary condition [9, 10, 12, 14].

2.2.2. Inflow/outflow boundary conditions

The configuration depicted in Fig. 1 raises a major issue of computational acoustics, i.e. the choice of the inflow and outflow boundary conditions. Among the methods consisting in adding a damping zone to the computational domain, we have chosen to use either Perfectly Matched Layer

(PML) boundary conditions first proposed by Bérenger [33] for computational electro-magnetics or more "standard" buffer zones [34, section 2.2.1]. Both methods consist in adding damping regions at the inflow and outflow, see Fig. 2.

As far as PML is concerned, we follow the work of Hu [35] where the reader can find further details. The method consists in applying an analytic continuation in the PML domain along the path:

$$x \to x + \mathrm{i}\frac{\Sigma(x)}{\omega} \ . \tag{4}$$

ω is the angular frequency and $\Sigma(x)$ is defined in the PML by Eq. (5).

$$\Sigma(x) = \begin{cases} \sigma_0 (x - x_0^d)^\alpha \text{ for } x > x_0 \\ -\sigma_0 (-x)^\alpha \text{ for } x < 0 \end{cases} \tag{5}$$

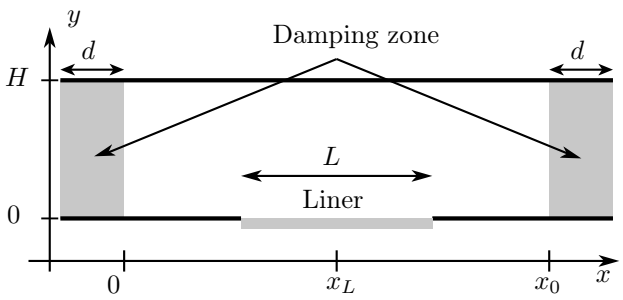

Figure 2: Schematic of the considered configuration with PML absorbing boundary condition.

It may be shown easily that this analytic continuation will indeed absorb a wave of angular frequency ω and wavenumber k if the phase velocity ω/k and the group velocity $\mathrm{d}\omega/\mathrm{d}k$ have the same sign[2]. On the contrary, if this condition is not satisfied, the wave is exponentially amplified in the PML domain. It is well-known that the linearised Euler equations may support waves that do not respect this condition. To get the PML stable, Hu [35] imposed a space-time transform of Prandtl-Glauert type defined by:

$$\mathring{t} = t + \tau x \ . \tag{6}$$

[2]This condition assumes that the group velocity gives the direction of propagation of a wave, although Brambley [12] showed that in some case "the sign of the group velocity is no longer conclusive in determining the direction of propagation".

For a uniform mean flow, $\tau = M^2/(1-M^2)$ is found analytically. For a shear flow of constant mean density, Hu [35] found empirically the following formula:

$$\tau = \frac{\bar{M}}{1-\bar{M}^2}. \tag{7}$$

The equations in the PML are then given according to the following steps:

i The linearised Euler equations Eqs. (1) are written in $(x, y, \mathring{t})$ by applying the space-time transform defined by Eq. (6).

ii The resulting equations are continued analytically in the frequency domain along the path defined by Eq. (4).

iii The equations are finally written back in (x, y, t).

The PML equations in time domain are:

$$\begin{cases} \partial_t \boldsymbol{\varphi} + \boldsymbol{A_j} \partial_j \boldsymbol{\varphi} + \boldsymbol{B}^{pml} \boldsymbol{\varphi} + \Sigma' \boldsymbol{A_y} \partial_y \boldsymbol{\phi} + \Sigma' \boldsymbol{B}\, \boldsymbol{\phi} = 0 \\ \partial_t \boldsymbol{\phi} = \boldsymbol{\varphi} \end{cases} \tag{8}$$

where $\boldsymbol{B}^{pml} = \boldsymbol{B} + \Sigma' \boldsymbol{I} + \Sigma' \tau \boldsymbol{A_x}$ ($\boldsymbol{I}$ is the identity matrix). The auxiliary variable $\boldsymbol{\phi}$ is only needed in the PML. In the frequency domain, Eq. (8) becomes:

$$(\mathrm{i}\omega)^2 \boldsymbol{\varphi} - \mathrm{i}\omega \left(\boldsymbol{A_j} \partial_j \boldsymbol{\varphi} + \boldsymbol{B}^{pml} \boldsymbol{\varphi} \right) + \Sigma' \boldsymbol{A_y} \partial_y \boldsymbol{\phi} + \Sigma' \boldsymbol{B}\, \boldsymbol{\phi} = 0 \tag{9}$$

Regarding buffer zones, this technique simply consists [34, section 2.2.1] in adding a damping term on the right-hand side of the governing equations. This term reads $-\Sigma(x)\boldsymbol{\varphi}$ (the damping function Σ follows Eq. (5)).

2.3. Configuration of Pascal et al. [31]

The configuration considered by Pascal et al. [31] consists in a lined duct carrying a streamwise invariant Poiseuille flow defined by Eq. (10) where the centerline Mach number is $M = 0.3$.

$$\frac{M_0}{M}(y) = 4\frac{(H-y)y}{H^2} \tag{10}$$

The impedance of the liner is set to $Z = 10^{-2}$. Even if this impedance is not representative of realistic liners, it satisfies the four conditions given by Rienstra [36] which ensure that an impedance model is physically realisable. Z has been chosen intentionally low since experimental investigations have

shown that hydrodynamic instabilities arise when the admittance is high [3, 5].

Pascal et al. [31] have shown by means of local linear stability analysis that the flow above the liner supports a convective hydrodynamic unstable wave. Local linear stability analysis consists in considering a perturbation written under the wave Ansatz $\exp(\mathrm{i}(k^j x - \omega t))\hat{\boldsymbol{\varphi}}^j(y)$. The local eigenmodes $\left(k_j, \hat{\boldsymbol{\varphi}}^j\right)$ are computed by solving the local eigenvalue problem:

$$-\mathrm{i}\omega\hat{\boldsymbol{\varphi}}^j + \boldsymbol{A_y}\partial_y\hat{\boldsymbol{\varphi}}^j + \boldsymbol{B}\hat{\boldsymbol{\varphi}}^j = \mathrm{i}k^j\boldsymbol{A_x}\hat{\boldsymbol{\varphi}}^j \ , \tag{11}$$

where $\hat{\boldsymbol{\varphi}}$ is subject to impedance boundary condition at $y = 0$ and hard wall boundary condition at $y = 1$. The figure 3 (taken from [31]) shows an example of computed spectrum. The hydrodynamic mode of eigenvalue k^g_{HI} has been shown to be amplified by means of the Briggs-Bers criterion (see [12, Appendix A] for clear and concise explanations). This mode reaches its highest growth rate for $\omega_{\max} = 4.41$. The flow supports as well a decaying hydrodynamic mode of wavenumber k^d_{HI} and acoustic modes, either left-running (of wavenumber k^{-j}_{AC}) or right-running (of wavenumber k^{+j}_{AC}).

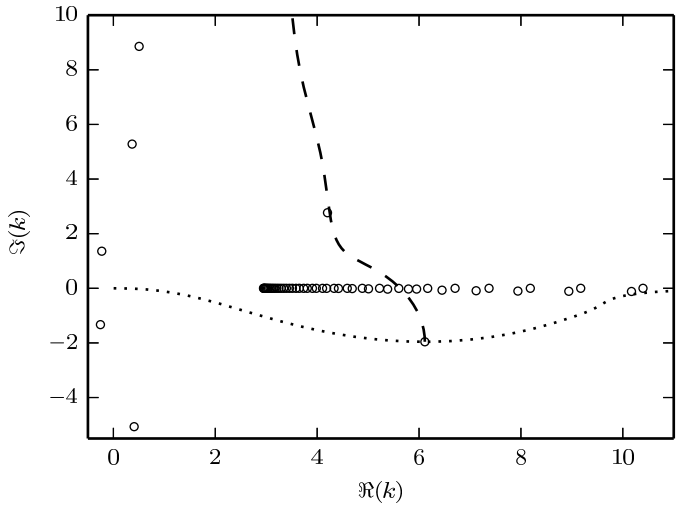

Figure 3: Spectrum for $\omega = \omega_{\max}$ taken from [31] (the reference length is here L). The dotted (respectively dashed) line corresponds to a tracking on $\Re(\omega)$ (respectively $\mathrm{Im}(\omega)$) of the amplified hydrodynamic eigenmode of eigenvalue k^g_{HI}.

Therefore, this configuration is an interesting toy model to study hydrodynamic instabilities that develop on acoustic lining. Moreover the computa-

tions of Pascal et al. [31] suggest that stable (respectively unstable) resonant dynamics might be observed for $L = 4$ ($L = 8$ respectively). This is shown in figures 4(a-b) (taken from [31]) where the energy $E(t) = \int_\Omega \boldsymbol{\varphi}(t)^2 \mathrm{d}\Omega$ (Ω is the physical domain) is plotted when the computation is initialised at $t = 0$ with a perturbation $\boldsymbol{\varphi}_0$ (obtained by optimal perturbation approach). For $L = 4$ pseudo-resonances are indeed observed, while for $L = 8$ the energy diverges.

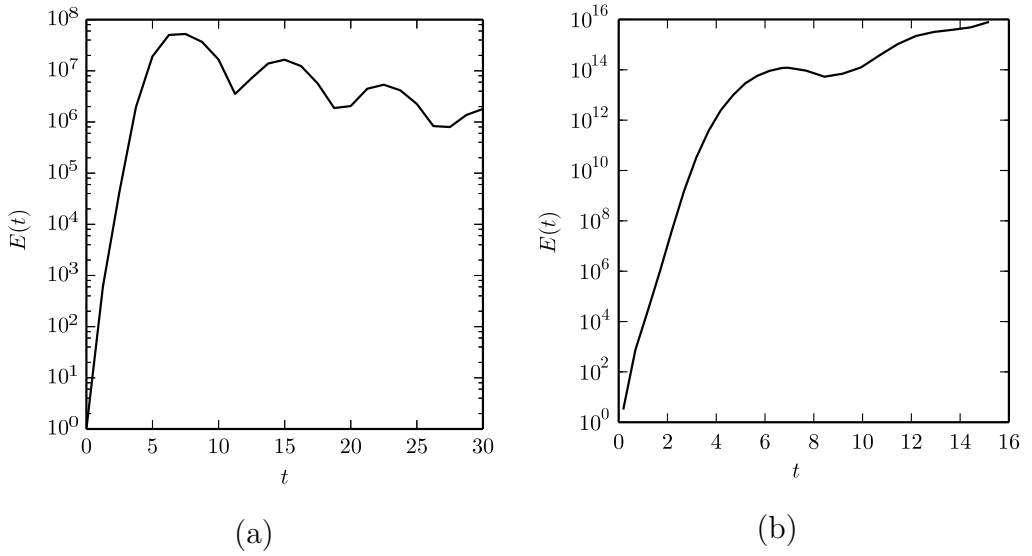

Figure 4: Time evolution of the energy E for $L = 4$ (a) and $L = 8$ (b), taken from [31] (the reference time is here $L/(a_0 M)$).

3. Numerical method

In this section the discontinuous Galerkin method used to discretise the governing equations is presented. For further details, the reader can consult Ref. [37].

3.1. Discretisation of the linearised Euler equations

The discretisation of Eq.(1) by the discontinuous Galerkin method is identical to the discretisation performed by Pascal et al. [31]. The solution is sought on each triangle $(D_l)_{l\in[\![1,N_l]\!]}$ in $P^2(D_l)$, the space of second order polynomial defined on D_l. The solution is found by imposing an orthogonality condition between the governing equations and the test-functions

$\boldsymbol{\psi}_m^l$ belonging to $P^2(D_l)$. The solution being locally defined on a triangle, numerical fluxes are imposed between neighbouring elements and to impose boundary conditions. Numerical fluxes are generally defined as functions of the solution in the triangle $\boldsymbol{\varphi}^-$ and in the neighbouring triangle $\boldsymbol{\varphi}^+$ and as a function of the vector normal to the triangle edge $\boldsymbol{n} = (n_x, n_y)$.

The discontinuous Galerkin formulation of Eq. (1) is similar to Pascal et al. [38, Eq. (7)] and reads:

$$\begin{aligned} &\forall l \in [\![1, N_l]\!], \forall \boldsymbol{\psi}_m^l \in P^2(D_l) \;\; \langle\, -\mathrm{i}\omega\boldsymbol{\varphi} + \boldsymbol{A_j}\partial_j\boldsymbol{\varphi} + \boldsymbol{B}\boldsymbol{\varphi}\,;\, \boldsymbol{\psi}_m^l \,\rangle_{D_l} \\ &+\langle\, [\boldsymbol{A_j} n_j]^- \left(\boldsymbol{\varphi}^+ - \boldsymbol{\varphi}^-\right)\,;\, \boldsymbol{\psi}_m^l \,\rangle_{\partial D_l \setminus \partial\Omega} + \langle\, \boldsymbol{M}(\beta)\boldsymbol{\varphi}^-\,;\, \boldsymbol{\psi}_m^l \,\rangle_{\partial D_l \cap \partial\Omega} = 0 \;. \end{aligned} \tag{12}$$

Where

$$\boldsymbol{M}(\beta) = \frac{1}{2}\begin{pmatrix} (\beta+1)n_x^2 & (\beta+1)n_x n_y & (\beta-1)n_x \\ (\beta+1)n_x n_y & (\beta+1)n_y^2 & (\beta-1)n_y \\ -(1+\beta)n_x & -(1+\beta)n_y & (1-\beta) \end{pmatrix} \;. \tag{13}$$

Definition of $[\boldsymbol{A}]^-$ for a matrix $\boldsymbol{A}$ is given in [31].

3.2. Discretisation with inflow/outflow boundary conditions

The discretisation of Eq. (9) follows the same reasoning and reads:

$$\begin{aligned} &\forall l \in [\![1, N_l]\!], \forall \boldsymbol{\psi}_m^l \in P^2(D_l) \;\; \langle\, (\mathrm{i}\omega)^2\,\boldsymbol{\varphi} - \mathrm{i}\omega\left(\boldsymbol{A_j}\partial_j\boldsymbol{\varphi} + \boldsymbol{B}^{pml}\boldsymbol{\varphi}\right) + \Sigma'\boldsymbol{A_y}\partial_y\boldsymbol{\varphi} + \Sigma'\boldsymbol{B}\,\boldsymbol{\varphi}\,;\, \boldsymbol{\psi}_m^l \,\rangle_{D_l} \\ &+\langle\, [\boldsymbol{A_j} n_j]^- \left(\boldsymbol{\varphi}^+ - \boldsymbol{\varphi}^-\right)\,;\, \boldsymbol{\psi}_m^l \,\rangle_{\partial D_l \setminus \partial\Omega} + \langle\, \boldsymbol{M}(\beta)\boldsymbol{\varphi}^-\,;\, \boldsymbol{\psi}_m^l \,\rangle_{\partial D_l \cap \partial\Omega} \\ &+\langle\, [\Sigma'\boldsymbol{A_y} n_y] \left(\boldsymbol{\varphi}^+ - \boldsymbol{\varphi}^-\right)\,;\, \boldsymbol{\psi_m^l} \,\rangle_{\partial D_l^{pml} \setminus \partial\Omega} + \langle\, \tilde{\boldsymbol{M}}\boldsymbol{\varphi}\,;\, \boldsymbol{\psi}_m^l \,\rangle_{\partial D_l^{pml} \cap \partial\Omega} = 0 \;, \end{aligned} \tag{14}$$

where

$$\tilde{\boldsymbol{M}} = \Sigma'\begin{pmatrix} 0 & 0 & 0 \\ 0 & n_y^2 & 0 \\ 0 & -n_y & 0 \end{pmatrix} \;.$$

If buffer domains are used the discretised equations read:

$$\begin{aligned} &\forall l \in [\![1, N_l]\!], \forall \boldsymbol{\psi}_m^l \in P^2(D_l) \;\; \langle\, -\mathrm{i}\omega\boldsymbol{\varphi} + \boldsymbol{A_j}\partial_j\boldsymbol{\varphi} + \boldsymbol{B}\boldsymbol{\varphi}\,;\, \boldsymbol{\psi}_m^l \,\rangle_{D_l} \\ &+\langle\, [\boldsymbol{A_j} n_j]^- \left(\boldsymbol{\varphi}^+ - \boldsymbol{\varphi}^-\right)\,;\, \boldsymbol{\psi}_m^l \,\rangle_{\partial D_l \setminus \partial\Omega} + \langle\, \boldsymbol{M}(\beta)\boldsymbol{\varphi}^-\,;\, \boldsymbol{\psi}_m^l \,\rangle_{\partial D_l \cap \partial\Omega} = -\langle\, \Sigma(x)\boldsymbol{\varphi}\,;\, \boldsymbol{\psi}_m^l \,\rangle_{D_l} \;. \end{aligned} \tag{15}$$

3.3. Eigenproblem solving

Eigenproblem (15) may be written under the global form

$$\boldsymbol{D}\boldsymbol{X} = \mathrm{i}\omega\boldsymbol{E}\boldsymbol{X} \ , \tag{16}$$

where the vector $\boldsymbol{X}$ contains all the degrees of freedom of the problem. The global linearised form of the quadratic eigenproblem eq. 14 is:

$$\begin{pmatrix} \boldsymbol{F} & \boldsymbol{0} \\ \boldsymbol{0} & \boldsymbol{I} \end{pmatrix} \begin{pmatrix} \boldsymbol{X} \\ \mathrm{i}\omega\boldsymbol{X} \end{pmatrix} = \mathrm{i}\omega \begin{pmatrix} \boldsymbol{G} & \boldsymbol{H} \\ \boldsymbol{I} & \boldsymbol{0} \end{pmatrix} \begin{pmatrix} \boldsymbol{X} \\ \mathrm{i}\omega\boldsymbol{X} \end{pmatrix} \ , \tag{17}$$

($\boldsymbol{I}$ is the identity matrix).

The eigenproblems (16) and (17) are solved by means of the Krylov-Schur method combined with shift-invert spectral transformation, implemented in the library `SLEPc` [39]. Such iterative method yields a few eigenvalues around a shift ω_σ. The shift is here chosen in the order of magnitude of $\bar{M}/L$.

The eigenmodes are normalised such that $p(x_L, 0) = 1$.

3.4. Mesh definition

The mesh is composed of triangles and is generated with `Gmsh` [40]. The global element size is $\Delta l = 1/20$. All along the liner, the mesh is refined by imposing the element size to be $\Delta l/4$. The mesh is further refined at the leading edge and trailing edge of the liner (element size of $\Delta l/10$ is imposed). It has been carefully checked that mesh is sufficiently refined for computing correctly the physically-relevant part of the spectrum.

The length of the hard-walled parts upstream and downstream of the liner is $x_L - L/2 = x_0 - (x_L + L/2) = 8$ (for instance for $L = 4$ and $L = 8$, $x_L = 10$ and $x_L = 12$ respectively).

4. Investigation of resonator dynamics

4.1. Modal computation on the configuration of Pascal et al. [31]

As proposed in the introduction, we are interested here in moving the configuration of Pascal et al. [31] from the time domain to the frequency domain. The computed eigenvalues ω are shown in figure 5(a) for $L = 4$ and in figure 5(b) for $L = 8$, for both PML and buffer domains boundary conditions. The parameters (damping rate, position, width) of the outflow boundary conditions have been varied to ensure that these artificial numerical

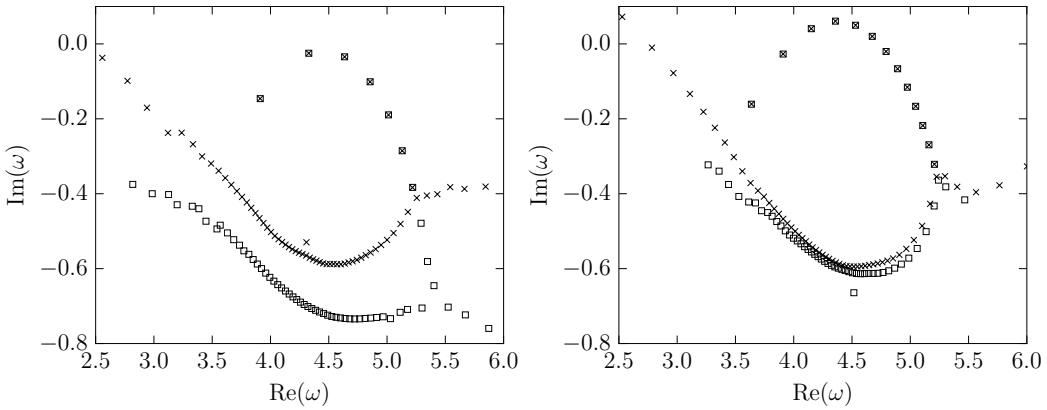

Figure 5: Spectrum for $L = 4$ (left) and $L = 8$ (right) with PML (cross symbol) or buffer domains (open square symbol).

boundaries do not pollute the solution in the physical computational domain.

For both values of L, only a few eigenvalues are independent of the type of damping zones used at the inflow and outflow. In the scope of the present study, they are the modes of interest as they are the physically relevant ones. As far as PML are concerned, the other modes have been described mathematically by Goursaud [41] (in French) and Kim [42]. Only eigenvalues obtained regardless of the type of damping zones within a relative accuracy of 10^{-3} are retained in the following.

The modal analysis presented in this section is in agreement with the time domain simulations performed by Pascal et al. [31]. Indeed figures 5(a-b) highlight that for $L = 4$ there are stable resonant modes (for all eigenvalues, $\mathrm{Im}(\omega) < 0$) while for $L = 8$ the system exhibits unstable resonator dynamics (some eigenvalues ω have a positive imaginary part). From the present modal analysis and from the results in the time domain of Pascal et al. [31], it can be concluded that the system dynamics moves from amplifier dynamics for $L = 4$ to resonator dynamics for $L = 8$.

For both values of L, the most unstable modes are obtained for frequencies close to ω_{max} (frequency leading to the highest growth rate according to spatial local linear stability analysis, see section 2.3).

4.2. Effect of the liner length

The physical modes for $L = \{4, 5, 6, 7, 8\}$ are shown in figure 6. Depending on the considered mode, the dependency on L might exhibit different characteristics. For instance the mode with $\omega \approx 4.33 - 0.02\mathrm{i}$ for $L = 4$ moves more across the complex plane than the mode with $\omega \approx 5.13 - 0.29\mathrm{i}$ for $L = 4$. As the modal stability of the system is primarily driven by the most amplified global modes, the highest temporal growth rate is plotted as a function of L in figure 7. Interestingly, the highest growth rate obeys quite well $0.15 - 0.69/L$ in the range $L \in [4, 8]$.

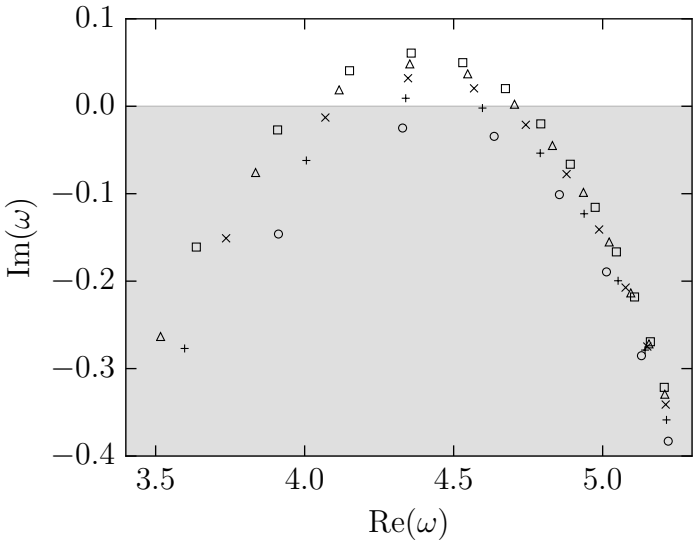

Figure 6: Spectrum for $L = 4$ (○), $L = 5$ (+), $L = 6$ (×) , $L = 7$ (△) and $L = 8$ (□). The unstable region is depicted in grey.

4.3. Eigenfunctions

From a qualitative point of view, the eigenfunctions of the most amplified eigenmode are barely modified when L is increased, see figures 8 and 9. These contours are similar to the snapshot of p shown by Pascal et al. [31, Fig. 3(b)]. The eigenfunctions are amplified along the liner and reach their highest values at the hard-soft lining transition. Therefore, it is of interest to plot $\Re(p)$ along the bottom wall such as in figures 10 and 11. Both figures are quite similar and are comparable to the snapshot of p on the lower wall computed by Pascal et al. [31, Fig. 4]. In both cases, the perturbation is

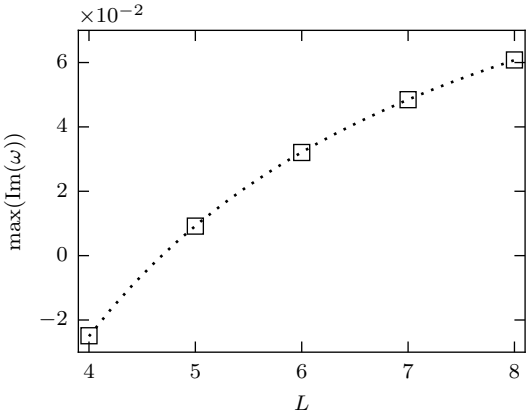

Figure 7: Highest temporal growth rate against the liner length. The dotted line corresponds to the function $0.15 - 0.69/L$.

amplified along the liner and exhibits a dramatic increase at the trailing edge, where maximal amplification is reached (the eigenfunctions are normalised such that $p(x_L, 0) = 1$, see section 3.3). The perturbation is then radiated with quite a high amplitude downstream of the liner while the perturbation is quite small upstream of the lined region. On the other hand, the perturbation is damped in the buffer domains. Since the perturbation is strongly amplified on the liner, figures 12(a,b) are displayed with a logarithm scale. Compared to $L = 4$, the perturbation exhibits a much higher amplification between the leading and trailing edges for $L = 8$.

5. Analysis of the spatial structure of global modes

This section is devoted to the understanding of the resonant mechanism. Since the flow above the liner has been shown not to be absolutely unstable by Pascal et al. [31] by means of the Briggs-Bers criterion, the resonator dynamics is not characterised by the existence of an absolutely unstable region but might result from a self-sustain mechanism associated to a feedback between local modes. Therefore we are investigating how local modes make up a global mode. Mathematically speaking, we are interested in finding a reconstruction of $\boldsymbol{\varphi}$, denoted $\boldsymbol{\varphi}^r$, based on a combination of local eigenfunctions ($\hat{\boldsymbol{\varphi}}^j$):

$$\boldsymbol{\varphi}^r(x, y) = \sum_j A^j \hat{\boldsymbol{\varphi}}^j(y) \exp\left(\mathrm{i}k^j x\right) \ . \tag{18}$$

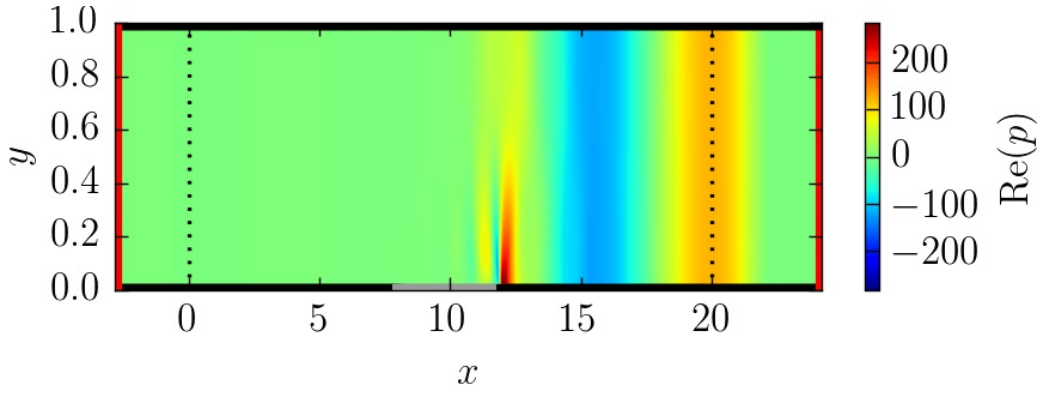

Figure 8: Real part of p-component of the most amplified eigenmode for $L = 4$. The lined section is in white, the vertical dotted lines depict the position of the buffer domains.

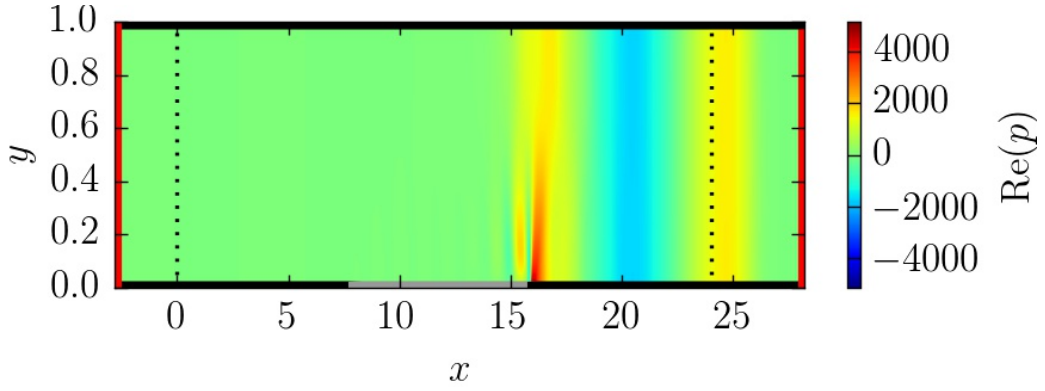

Figure 9: Real part of p-component of the most amplified eigenmode for $L = 8$. The lined section is in white, the vertical dotted lines depict the position of the buffer domains.

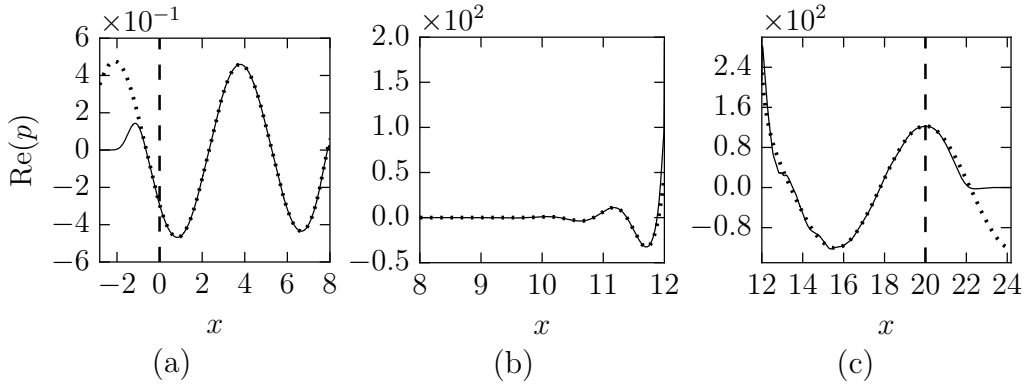

Figure 10: Real part of p-component of the most amplified eigenmode for $L = 4$ along the lower wall (left: upstream rigid wall, middle: lined wall, right: downstream rigid wall). Vertical dashed lines depict the position of the buffer domains. Reconstruction by means of biorthogonal projection (see section 5) are plotted with dotted lines.

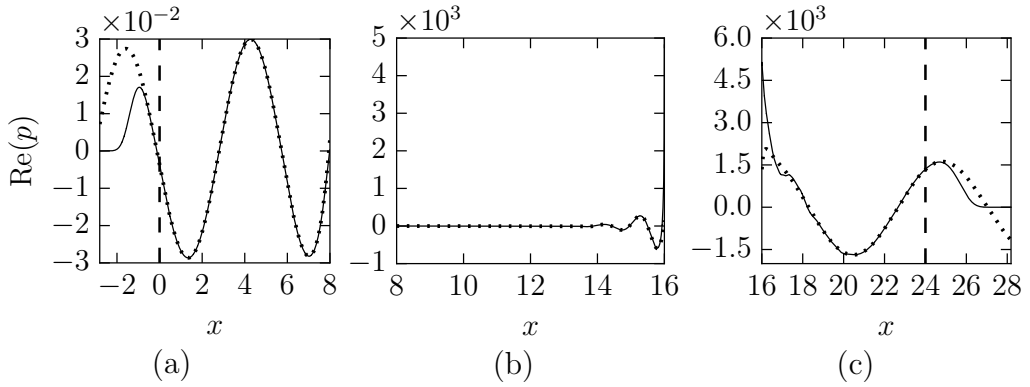

Figure 11: Real part of p-component of the most amplified eigenmode for $L = 8$ along the lower wall (left: upstream rigid wall, middle: lined wall, right: downstream rigid wall). Vertical dashed lines depict the position of the buffer domains. Reconstruction by means of biorthogonal projection (see section 5) are plotted with dotted lines.

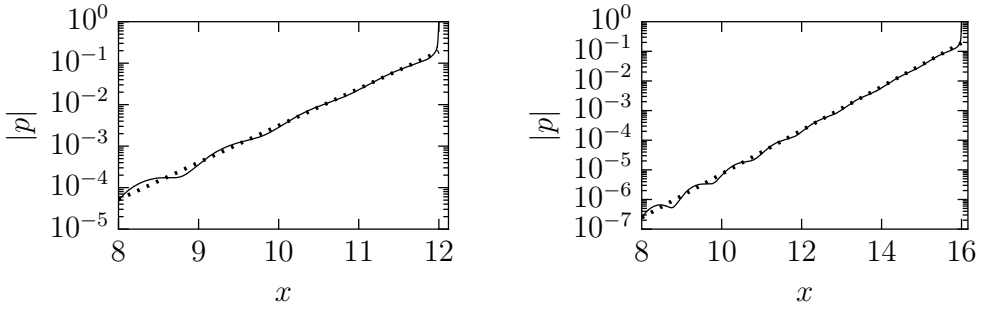

(a) (b)

Figure 12: Modulus of p-component of the most amplified eigenmode for $L = 4$ (a) and $L = 8$ (b) on the liner. Reconstruction by means of biorthogonal projection (see section 5) are plotted with dotted lines

5.1. Biorthogonal decomposition

Getting the amplitude A_j of a given mode in Eq. (18) from $\boldsymbol{\varphi}$ is not straightforward since the local eigenvectors $\hat{\boldsymbol{\varphi}}^j$ form a non-orthogonal basis. To circumvent this difficulty, the biorthogonal decomposition technique is used. This technique, detailed in Appendix A, has been successfully applied for modes in wall jet and boundary layer flows [43, 44, 45]. It relies on a specific scalar product involving the local direct and adjoint local eigenfunctions.

In the following, $\boldsymbol{\varphi}$ corresponds to the eigenfunction of the most amplified global mode and only the cases $L = 4$ and $L = 8$ are considered for which $x_L = 10$ and $x_L = 12$ respectively. Hence, the local modes $\left(k^j, \hat{\boldsymbol{\varphi}}^j\right)$ are computed by solving Eq. (11) with $\omega = 4.33 - 0.025\mathrm{i}$ for $L = 4$ and $\omega = 4.36 + 0.061\mathrm{i}$ for $L = 8$.

5.1.1. In the lined region

In the lined region $x \in [x_L - L/2, x_L + L/2]$, $\boldsymbol{\varphi}^r$ is expressed as:

$$\begin{aligned}\boldsymbol{\varphi}^r(x,y) = A^g_{HI}\hat{\boldsymbol{\varphi}}^g_{HI}(y)\exp\left(\mathrm{i}k^g_{HI}x\right) + A^d_{HI}\hat{\boldsymbol{\varphi}}^d_{HI}(y)\exp\left(\mathrm{i}k^d_{HI}x\right) + \\ \sum_{j=0}^{N^+_{AC}} A^{+j}_{AC}\hat{\boldsymbol{\varphi}}^{+j}_{AC}(y)\exp\left(\mathrm{i}k^{+j}_{AC}x\right) + \sum_{j=0}^{N^-_{AC}} A^{-j}_{AC}\hat{\boldsymbol{\varphi}}^{-j}_{AC}(y)\exp\left(\mathrm{i}k^{-j}_{AC}x\right)\end{aligned} \tag{19}$$

As shown on the spectrum in figure 3, the parameters labeled $(\cdot)^g_{HI}$ (respectively $(\cdot)^d_{HI}$) are related to the growing (respectively decaying) hydrody-

	$L = 4$ ($\omega = 4.33 - 0.025\mathrm{i}$)	$L = 8$ ($\omega = 4.36 + 0.061\mathrm{i}$)
k^g_{HI}	$5.74 - 2.05\mathrm{i}$	$5.88 - 1.70\mathrm{i}$
k^{-0}_{AC}	$-0.25 - 1.34\mathrm{i}$	$-0.26 - 1.34\mathrm{i}$

Table 1: Wavenumbers k^g_{HI} and k^{-0}_{AC} solution of Eq. (11) for ω corresponding to the most unstable global mode.

namic local mode. The label AC corresponds to acoustic modes, the sign $+$ (respectively $-$) refers to right-running (respectively left-running mode). $N^+_{AC} = 2$ and $N^-_{AC} = 3$ is chosen (therefore "all modes" will refer to a combination of the local modes of wavenumbers $k^g_{HI}, k^d_{HI}, k^{+0}_{AC}, k^{+1}_{AC}, k^{+2}_{AC}, k^{-0}_{AC}, k^{-1}_{AC}, k^{-2}_{AC}, k^{-3}_{AC}$). Table 1 gives the wavenumbers k^g_{HI} and k^{-0}_{AC} for $L = 4$ and $L = 8$ (it will be seen in the following that these two modes are of particularly great interest).

For $L = 4$ (respectively $L = 8$), the pressure component of $\boldsymbol{\varphi}^r$ is compared to p in figures 10(b) and 12(a) (respectively figures 11(b) and 12(b)). An almost perfect match is obtained. In order to perform more accurate comparisons, the relative error between $\boldsymbol{\varphi}$ and $\boldsymbol{\varphi}^r$ is plotted figure 13 for $L = 4$ and figure 14 for $L = 8$. For both liner lengths, the results are similar from a qualitative point of view. $\boldsymbol{\varphi}^r$ matches well $\boldsymbol{\varphi}$ for $x_L - L/2 + 2 \lesssim x \lesssim x_L + L/2 - 1$. In order to estimate the contribution of each mode, additional reconstructions are computed where the modes accounted for are changed, see figures 13 and 14. Far from the liner edges, considering only k^g_{HI} and k^{-0}_{AC} is enough to accurately approximate $\boldsymbol{\varphi}$ while considering only one of them leads to a poor agreement. On the contrary, neglecting these two modes yields a high deviation between $\boldsymbol{\varphi}$ and $\boldsymbol{\varphi}^r$.

In order to gain a better insight into the behaviour at the liner trailing edge, a close-up is shown figure 15(a) for $L = 4$. As more and more left-running acoustic modes of higher order are accounted for, a better agreement between $\boldsymbol{\varphi}^r$ and $\boldsymbol{\varphi}$ is obtained. This statement is only partially true for $L = 8$, see figure 15(b), since accounting for the mode k^{-3}_{AC} does not improve the matching [3].

Similarly, figures 16(a-b) show a close-up at the liner leading edge. From a qualitative point of view, adding high-order right-running acoustic mode re-

[3] Actually, this seems to be due to the very high amplification along the liner for $L = 8$ (see figure 12) which in this case get the solution close to numerical overflow. For $L = 6$ (not shown here), adding the mode of wavenumber k^{-3}_{AC} indeed improves the matching between $\boldsymbol{\varphi}^r$ and $\boldsymbol{\varphi}$, as for $L = 4$.

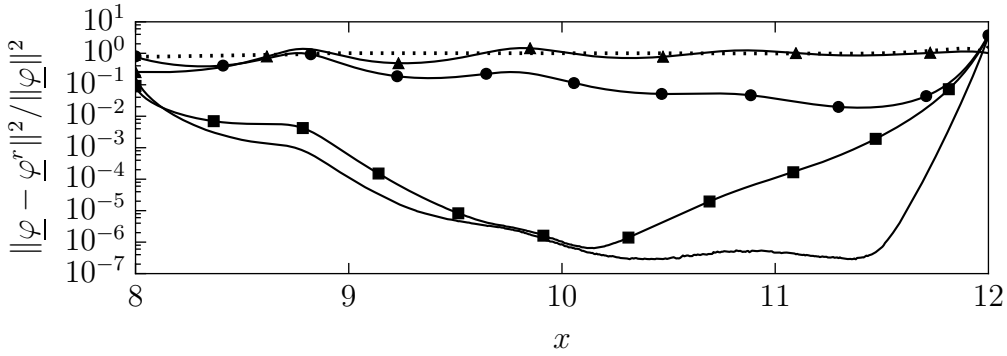

Figure 13: Relative deviation between $\boldsymbol{\varphi}$ and $\boldsymbol{\varphi}^r$ in the lined region for $L = 4$.
—— all modes —●— k^g_{HI} —■— k^g_{HI} and k^{-0}_{AC}
····· all modes but k^g_{HI} and k^{-0}_{AC} —▲— k^{-0}_{AC}

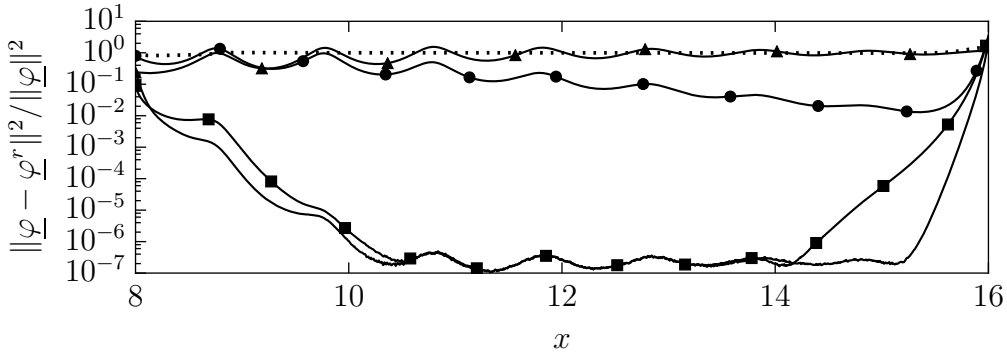

Figure 14: Relative deviation between $\boldsymbol{\varphi}$ and $\boldsymbol{\varphi}^r$ in the lined region for $L = 8$.
See the legend figure 13

duces the deviation between the reconstructed field and the computed eigenfunction. However, from a quantitative point of view, this effect is not as strong as at the trailing edge as only a slight improvement is observed. All these results explain why it was chosen to limit to $N_{AC}^{+} = 2$ and $N_{AC}^{-} = 3$ the number of acoustic modes in the reconstruction.

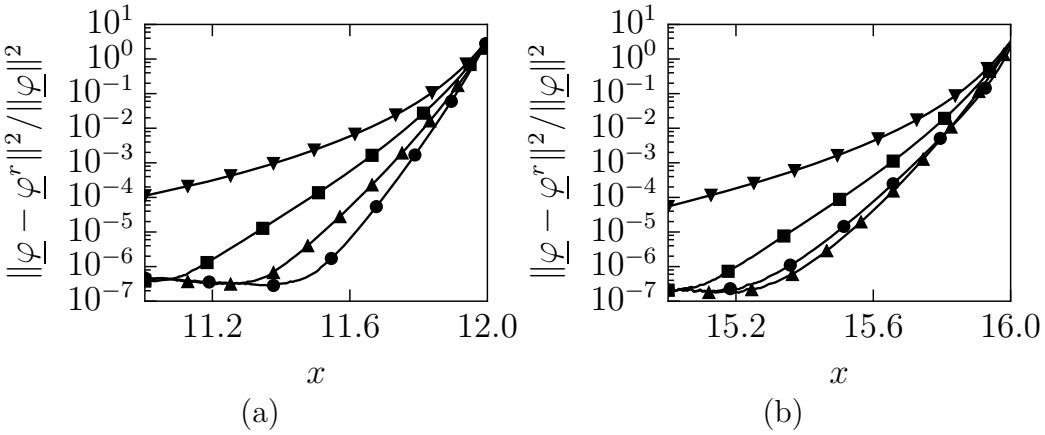

Figure 15: Relative deviation between $\boldsymbol{\varphi}$ and $\boldsymbol{\varphi}^r$ in the lined region near the trailing edge for $L = 4$ (a) and $L = 8$(b).

—●— all modes —▲— all modes but k_{AC}^{-3}
—■— all modes but k_{AC}^{-2} and k_{AC}^{-3} —▼— all modes but k_{AC}^{-1}, k_{AC}^{-2} and k_{AC}^{-3}

5.1.2. In the rigid parts

In the rigid part, there is no hydrodynamic (discrete) local mode and the reconstruction is expressed as:

$$\boldsymbol{\varphi}^r(x,y) = \sum_{j=0}^{N_{AC}^{+}} A_{AC}^{+j} \hat{\boldsymbol{\varphi}}_{AC}^{+j}(y) \exp\left(\mathrm{i}k_{AC}^{+j}x\right) + \sum_{j=0}^{N_{AC}^{-}} A_{AC}^{-j} \hat{\boldsymbol{\varphi}}_{AC}^{-j}(y) \exp\left(\mathrm{i}k_{AC}^{-j}x\right) \quad (20)$$

For the sake of clarity, the same labels as in Eq. (19) are used even if they correspond to modes subject to hard wall boundary condition. $k_{AC}^{\pm j}$, $\hat{\boldsymbol{\varphi}}_{AC}^{\pm j}$ and $A_{AC}^{\pm j}$ are not the same as in Eq. (19).

In the upstream region ($x \leq x_L - L/2$), the projection is performed only on left-running acoustic modes: $N_{AC}^{-} = 4$ and $N_{AC}^{+} = 0$ is chosen, see figures 17(a-b). Excepted in the vicinity of the liner leading edge, the reconstruction matches well the computed eigenfunction. Accounting for the

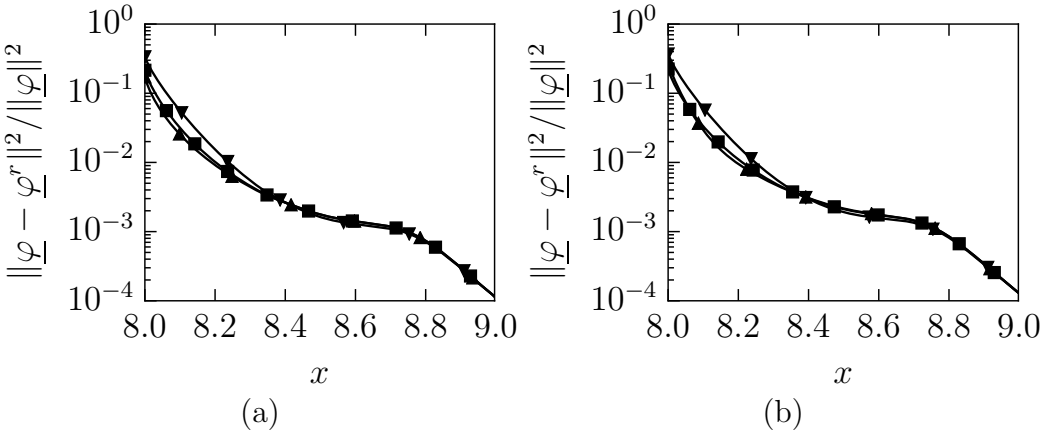

Figure 16: Relative deviation between $\boldsymbol{\varphi}$ and $\boldsymbol{\varphi}^r$ in the lined region near the leading edge for $L = 4$ (a) and $L = 8$(b).

all modes — all modes but k_{AC}^{+2} — all modes but k_{AC}^{+1} and k_{AC}^{+2}

acoustic mode of wavenumber k_{AC}^{-0} is a necessary condition for $\boldsymbol{\varphi}^r$ to match $\boldsymbol{\varphi}$. Taking into account left-running modes of higher order gradually reduces the deviation between $\boldsymbol{\varphi}^r$ and $\boldsymbol{\varphi}$ near hard-soft junction.

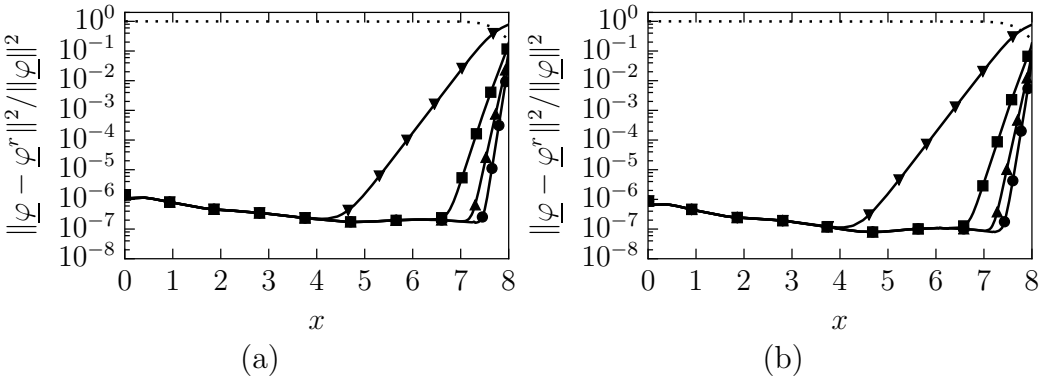

Figure 17: Relative deviation between $\boldsymbol{\varphi}$ and $\boldsymbol{\varphi}^r$ in the upstream hard-walled part for $L = 4$ (a) and $L = 8$(b).

k_{AC}^{-1}, k_{AC}^{-2} and k_{AC}^{-3} — k_{AC}^{-0} — k_{AC}^{-0}, k_{AC}^{-1}, k_{AC}^{-2} and k_{AC}^{-3}

k_{AC}^{-0}, k_{AC}^{-1} and k_{AC}^{-2} — k_{AC}^{-0} and k_{AC}^{-1}

In the downstream region ($x \geq x_L + L/2$), the projection is performed only on right-running acoustic modes: $N_{AC}^{+} = 4$ and $N_{AC}^{-} = 0$ is chosen, see

figures 18(a-b) and 19(a-b). Accounting for k_{AC}^{+0} appears to be a necessary condition for $\boldsymbol{\varphi}^r$ to match $\boldsymbol{\varphi}$. The behaviour in the vicinity of the liner trailing edge is quite surprising as increasing the number of modes does not lead to a better agreement. As x increases and leaves the vicinity of $x_L + L/2$, the relative deviation is independent of the number of high-order acoustic modes and decreases gradually.

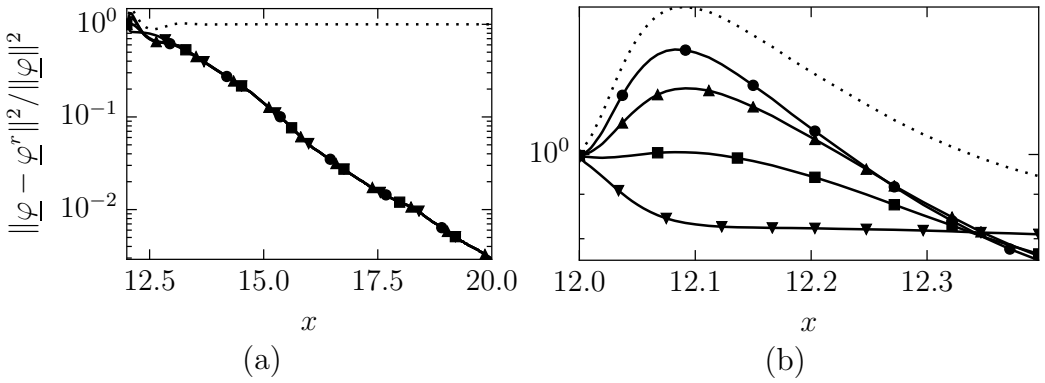

Figure 18: Relative deviation between $\boldsymbol{\varphi}$ and $\boldsymbol{\varphi}^r$ in the downstream hard-walled part for $L = 4$.

..... k_{AC}^{+1}, k_{AC}^{+2} and k_{AC}^{+3} —▼— k_{AC}^{+0} —●— k_{AC}^{+0}, k_{AC}^{+1}, k_{AC}^{+2} and k_{AC}^{+3}
—▲— k_{AC}^{+0}, k_{AC}^{+1} and k_{AC}^{+2} —■— k_{AC}^{+0} and k_{AC}^{+1}

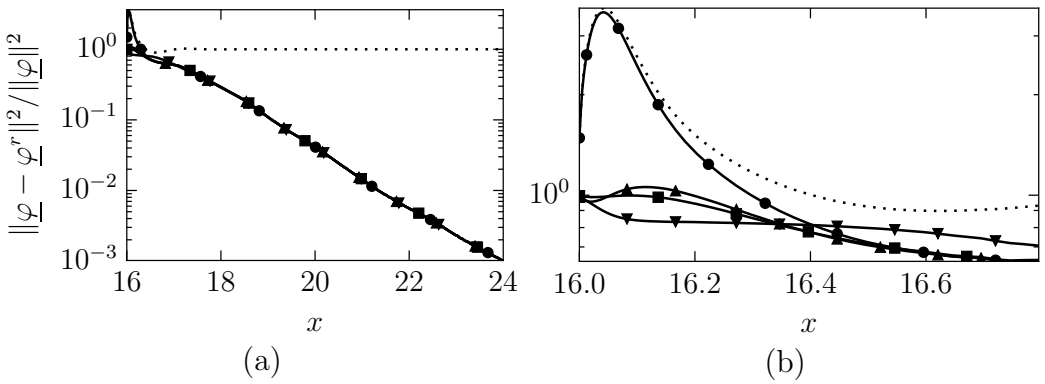

Figure 19: Relative deviation between $\boldsymbol{\varphi}$ and $\boldsymbol{\varphi}^r$ in the downstream hard-walled part for $L = 8$.

See the legend figure 18

5.2. Discussion

Figures 13 and 14 shows that, excepted near the liner edges, the perturbation is made up of the hydrodynamic unstable mode (of wavenumber k^g_{HI}) and of the first left-running acoustic mode (of wavenumber k^{-0}_{AC}). Near the liner trailing edge ($x = x_L + L/2$), left-running acoustic waves of higher order are significant which is in agreement with the statement of Alomar and Aurégan [6, section 4.2.1]: "higher order modes are important [...] only in the immediate vicinity of the liner edges", see figures 16(a-b). Left-running acoustic modes result from the scattering of the hydrodynamic wave at the trailing edge of the liner and the peak at $x = x_L + L/2$ seen figures 10(b) and 11(b) actually correspond to the exponential decay of high-order left-running evanescent acoustic mode of (initially) high amplitude. In the vicinity of the liner leading edge, accounting for higher order right-running acoustic waves barely improves the matching between the reconstruction and the global eigenfunction as shown figures 16(a-b). Moreover, the domain of influence of the liner leading edge (about 2) is greater than the domain of influence of the liner trailing edge (less than about 1). This different behaviour at the upstream edge might be explain by the scattering of the first left-running acoustic mode into hydrodynamic modes belonging to the continuous spectrum, which are not accounted for in the reconstruction defined by Eq. (19) and whose contribution is known to decay following an algebraic function of x [46].

In the hard-walled part upstream of the liner, the global mode is primarily composed by the first left-running acoustic mode as reported by Pascal et al. [31]. Near the liner upstream edge ($x = x_L - L/2 - \varepsilon$), the higher order left-running acoustic modes are also important, see figures 17(a-b). These left-running acoustic modes result from the scattering of the first left-running acoustic mode propagating over the liner, which is quite similar to the behaviour observed for $x = x_L + L/2 - \varepsilon$.

The behaviour of the perturbation downstream of the liner edges ($x \geq x_L + L/2$) is more complex. While the first right-running acoustic mode plays an important role, as reported by Pascal et al. [31], simply adding acoustic modes of higher order in the reconstruction is not enough to get a satisfactory matching with the global eigenfunction. As explained previously for $x_L - L/2 \leq x \lesssim x_L - L/2 + 2$, the algebraic decay rate associated to the modes of the continuous spectrum (whose contribution is not accounted for in the reconstruction defined by Eq. (20)) might explain why the deviation between $\boldsymbol{\varphi}^r$ and $\boldsymbol{\varphi}$ gradually decreases as x is increased downstream of the

liner. Both the right-running acoustic mode and the modes associated to the continuous spectrum result from the scattering of the hydrodynamic unstable wave propagating over in the lined region at the liner trailing edge.

Biorthogonal projection proves that the global instability mode is mainly composed of the hydrodynamic unstable wave and the first left-running acoustic mode. As the flow above the liner has been shown not to be absolutely unstable, the self-sustain oscillations characterising the resonator dynamics are to be explained as resulting from a feedback mechanism. In the following, a feedback scenario in the lined section is proposed between the hydrodynamic unstable wave and the first left-running acoustic mode. The former would grow along the liner with the growth rate $-\mathrm{Im}\left(k_{HI}^{g}\right)$ and would be scattered off into the latter as it reaches eventually the liner trailing edge. The acoustic mode would then propagate upstream, while being damped with the rate $\mathrm{Im}\left(k_{AC}^{-0}\right)$, and reaches the liner leading edge where it scatters off back into the amplified hydrodynamic wave. In addition to the fact that both modes scatter off into each other at the liner edges, a key condition that would explain the resonator dynamics is the fact that the growth rate of the hydrodynamic wave is greater than the damping rate of the left-running acoustic mode, as seen in figure 3 and table 1.

As the liner is enlengthened, the perturbation is more and more amplified between the liner leading edge and trailing edge (see figure 12), following the trend given by the hydrodynamic instability growth rate. Intuitively, the resonator dynamics might then switch from stable to unstable if the losses associated to the scattering at both edges and the decay of the left-running acoustic mode are not sufficient to counterbalance this increase.

The existence of a feedback associated to hard/lined transitions has been reported in the time domain studies of Pascal et al. [31] and Marx [47]. The latter considers as well a case where the aforementioned condition $-\mathrm{Im}(k_{HI}^{g}) > -\mathrm{Im}(k_{AC}^{-0})$ is satisfied (as seen [47, figure 3]) and the author even raises the possibility that this feedback might lead to global unstable behaviour (without observing it numerically).

While the configuration considered in this paper represents a nice toy model to study hydrodynamic instability phenomenon in lined flow duct, it would be interesting to perform similar studies with more realistic base flows and impedance laws. The implementation of the Extended Helmholtz Resonator proposed by Pascal et al. [48] or the use of an oscillatory-diffusive

representation [49] offer the possibility to keep the eigenproblem linear with respect to ω even for non-linear impedance laws. Moreover, it would be interesting for instance to take into account viscosity as it has been shown to have a significant impact on lined flow duct stability [22]. Non-linear effects are as well expected to be significant through the saturation of the perturbation amplification.

6. Conclusion

Global stability analysis in a lined duct has been performed using the linearised Euler equations in presence of shear flow. The latter are discretised by means of discontinuous Galerkin method and the resulting generalised eigenproblem is solved by means of iterative method. The linearised Euler equations in a lined channel are shown to support global modes on a toy model configuration. As the liner is enlengthened, the temporal growth rate increases and the system switches from globally stable to globally unstable. These results obtained by means of modal analysis are in agreement with the study of Pascal et al. [31] performed in the time domain. How local modes make up global modes has been investigated by means of biorthogonal projection. In particular, global instability has been shown to be related to hydrodynamic-acoustic feedback at hard/soft junctions.

Appendix A. Biorthogonal projection

Tumin et al. [43] applied the biorthogonal decomposition to experimental data of 2-D wall jet configuration. This technique offers a way to decompose $\boldsymbol{\varphi}$ onto the (non-normal) basis of local spatial modes by using adjoint modes as projectors. These modes satisfy:

$$\begin{cases} \boldsymbol{L}\hat{\boldsymbol{\varphi}}^j - k^j \boldsymbol{N}\hat{\boldsymbol{\varphi}}^j = 0 \\ \boldsymbol{L}^H\hat{\boldsymbol{\psi}}^l - \bar{k^l}\boldsymbol{N}^H\hat{\boldsymbol{\psi}}^l = 0 \end{cases} \tag{A.1}$$

where $(\cdot)^H$ and $\bar{(\cdot)}$ denote respectively transconjugate and complex conjugate, $\boldsymbol{N} = \mathrm{i}\boldsymbol{A_x}$ and $\boldsymbol{L} = -\mathrm{i}\omega + \boldsymbol{A_y}\partial_y + \boldsymbol{B}$ (Eq. (11)). $\hat{\boldsymbol{\psi}}^l$ is the adjoint eigenfunction.

Appendix A.1. Biorthogonal relationship

The biorthogonal relationship is derived from the expression:

$$\langle \left(\boldsymbol{L} - k^j\boldsymbol{N}\right)\hat{\boldsymbol{\varphi}}^j \,;\, \hat{\boldsymbol{\psi}}^l \rangle_{y\in[0,1]} - \langle \hat{\boldsymbol{\varphi}}^j \,;\, \left(\boldsymbol{L}^H - \bar{k^l}\boldsymbol{N}^H\right)\hat{\boldsymbol{\psi}}^l \rangle_{y\in[0,1]} = 0 \ , \tag{A.2}$$

where $\langle\, \boldsymbol{a}\,;\,\boldsymbol{b}\,\rangle_{y\in[0,1]}$ is the standard scalar product $\displaystyle\int_0^1 \boldsymbol{a}\cdot\bar{\boldsymbol{b}}\;\mathrm{d}y$. Eq. (A.2) might be written:

$$\langle\, \left(\boldsymbol{L}-k^j\boldsymbol{N}\right)\hat{\boldsymbol{\varphi}}^j-\left(\boldsymbol{L}-k^l\boldsymbol{N}\right)\hat{\boldsymbol{\varphi}}^j\,;\,\hat{\boldsymbol{\psi}}^l\,\rangle_{y\in[0,1]}=0, \tag{A.3}$$

which yields the biorthogonal relationship:

$$\left(k^l-k^j\right)\langle\, \boldsymbol{N}\hat{\boldsymbol{\varphi}}^j\,;\,\hat{\boldsymbol{\psi}}^l\,\rangle_{y\in[0,1]}=0. \tag{A.4}$$

Appendix A.2. Biorthogonal decomposition

Let $\boldsymbol{\phi}(y)$ be a combination of local modes:

$$\boldsymbol{\phi}(y)=\sum_j K^j\hat{\boldsymbol{\varphi}}^j(y)\;, \tag{A.5}$$

the biorthogonal relationship Eq. (A.4) yields:

$$\langle\, \boldsymbol{N}\boldsymbol{\phi}\,;\,\hat{\boldsymbol{\psi}}^l\,\rangle_{y\in[0,1]}=K^l\langle\, \boldsymbol{N}\hat{\boldsymbol{\varphi}}^{\boldsymbol{l}}\,;\,\hat{\boldsymbol{\psi}}^l\,\rangle_{y\in[0,1]}\;. \tag{A.6}$$

Finally, the amplitude K^j associated to the local mode $(k^j,\hat{\boldsymbol{\varphi}}^j)$ in Eq. (A.5) is then given by:

$$K^j=\frac{\langle\, \boldsymbol{N}\boldsymbol{\phi}\,;\,\hat{\boldsymbol{\psi}}^j\,\rangle_{y\in[0,1]}}{\langle\, \boldsymbol{N}\hat{\boldsymbol{\varphi}}^{\boldsymbol{j}}\,;\,\hat{\boldsymbol{\psi}}^j\,\rangle_{y\in[0,1]}}\;. \tag{A.7}$$

Appendix A.3. Application to $\boldsymbol{\varphi}(x,y)$

This section is intended to show how the biorthogonal decomposition technique is applied to compute the complex amplitude A^j in Eq. (18) . The global eigenfunction $\boldsymbol{\varphi}(x,y)$ is a linear combination of local modes:

$$\boldsymbol{\varphi}(x,y)=\sum_j A^j\hat{\boldsymbol{\varphi}}^j(y)\exp\left(\mathrm{i}k^jx\right)\;. \tag{A.8}$$

Let P^j be defined by:

$$P^j(x)=\frac{\langle\, \boldsymbol{N}\boldsymbol{\varphi}(x,y)\,;\,\hat{\boldsymbol{\psi}}^j\,\rangle_{y\in[0,1]}}{\langle\, \boldsymbol{N}\hat{\boldsymbol{\varphi}}^{\boldsymbol{j}}\,;\,\hat{\boldsymbol{\psi}}^j\,\rangle_{y\in[0,1]}}\;. \tag{A.9}$$

The biorthogonal relationship yields:

$$P^j(x) = A^j \exp(\mathrm{i}k^j x) \ , \tag{A.10}$$

or:

$$A^j = P^j(x) \exp\left(-\mathrm{i}k^j x\right) \ . \tag{A.11}$$

On the contrary to what is obtained with a standard least-squares decomposition, the same amplitude A^j is obtained whatever the total number of modes used in the decomposition.

References

1. Meyer, E. , Mechel, F. , Kurtze, G. . Experiments on the influence of flow on sound attenuation in absorbing ducts. *The Journal of the Acoustical Society of America* 1958;30(3):165–174.

2. Brandes M, Ronneberger D. Sound amplification in flow ducts lined with a periodic sequence of resonators. In: *1st AIAA/CEAS Aeroacoustics Conference*. AIAA-95-126; 1995:893–901.

3. Jüschke M. Akustische Beeinflussung einer Instabilität in Kanälen mit überströmten Resonatoren [Acoustic influence on an instability in a yielding-walled flow duct section]. Ph.D. thesis; Niedersächsische Staats- und Universitätsbibliothek Göttingen; 2006.

4. Aurégan Y, Leroux M. Experimental evidence of an instability over an impedance wall in a duct with flow. *Journal of Sound and Vibration* 2008;317(3):432–439.

5. Marx D, Aurégan Y, Bailliet H, Valière JC. PIV and LDV evidence of hydrodynamic instability over a liner in a duct with flow. *Journal of Sound and Vibration* 2010;329(18):3798–3812.

6. Alomar A, Aurégan Y. Particle image velocimetry measurement of an instability wave over a porous wall in a duct with flow. *Journal of Sound and Vibration* 2017;386:208–224.

7. Li XD, Richter C, Thiele F. Time-domain impedance boundary conditions for surfaces with subsonic mean flows. *The Journal of the Acoustical Society of America* 2006;119(5):2665–2676.

8. Burak MO, Billson M, Eriksson LE, Baralon S. Validation of a time- and frequency-domain grazing flow acoustic liner model. *AIAA Journal* 2009;47:1841–1848.

9. Ingard U. Influence of fluid motion past a plane boundary on sound reflection, absorption, and transmission. *The Journal of the Acoustical Society of America* 1959;31(7):1035–1036.

10. Myers M. On the acoustic boundary condition in the presence of flow. *Journal of Sound and Vibration* 1980;71(3):429–434.

11. Rienstra S. A classification of duct modes based on surface waves. *Wave Motion* 2003;37(2):119 – 135.

12. Brambley EJ. Fundamental problems with the model of uniform flow over acoustic linings. *Journal of Sound Vibration* 2009;322:1026–1037.

13. Rienstra S, Darau M. Boundary-layer thickness effects of the hydrodynamic instability along an impedance wall. *Journal of Fluid Mechanics* 2011;671:559–573.

14. Brambley E. A well-posed boundary condition for acoustic liners in straight ducts with flow. *AIAA Journal* 2011;49(6):1272–1282.

15. Brambley E. Review of acoustic liner models with flow. In: *Acoustics 2012 Nantes*. 2012:3423–3428.

16. Gabard G. A comparison of impedance boundary conditions for flow acoustics. *Journal of Sound And Vibration* 2013;332:714–724.

17. Brambley E. Surface modes in sheared boundary layers over impedance linings. *Journal of Sound and Vibration* 2013;332:3750–3767.

18. Rienstra S, Vilenski G. Spatial instability of boundary layer along impedance wall. In: *AIAA/CEAS Aeroacoustics Conference*. AIAA-2008-2932; 2008:1–13.

19. Marx D, Aurégan Y. Comparison of experiments with stability analysis prediction in a lined flow duct. In: *16th AIAA/CEAS Aeroacoustics Conference*. AIAA-2010-3946; 2010:1–17.

20. Boyer G, Piot E, Brazier JP. Theoretical investigation of hydrodynamic surface mode in a lined duct with sheared flow and comparison with experiment. *Journal of Sound and Vibration* 2011;330(8):1793 – 1809.

21. Marx D, Aurégan Y. Effect of turbulent eddy viscosity on the unstable surface mode above an acoustic liner. *Journal of Sound and Vibration* 2013;332(15):3803–3820.

22. Khamis D, Brambley EJ. Viscous effects on the acoustics and stability of a shear layer over an impedance wall. *Journal of Fluid Mechanics* 2017;810:489–534.

23. Koch W, Moehring W. Eigensolutions for liners in uniform mean flow ducts. *AIAA Journal* 1983;21(2):200–213.

24. Theofilis V. Global linear instability. *Annual Review of Fluid Mechanics* 2011;43:319–352.

25. Schmid PJ, Henningson DS. Stability and transition in shear flows; vol. 142. Springer Science & Business Media; 2012.

26. Huerre P, Rossi M. Hydrodynamics and Nonlinear Instabilities; chap. Hydrodynamic instabilities in open flow. Godreche, C. and Manneville P., Cambridge University press; 1998:81–294.

27. Ehrenstein U, Gallaire F. On two-dimensional temporal modes in spatially evolving open flows: the flat-plate boundary layer. *Journal of Fluid Mechanics* 2005;536:209–218.

28. Marquet O, Sipp D, Chomaz JM, Jacquin L. Amplifier and resonator dynamics of a low-reynolds-number recirculation bubble in a global framework. *Journal of Fluids Mechanics* 2008;605:429–443.

29. Sipp D, Marquet O. Characterization of noise amplifiers with global singular modes: the case of the leading-edge flat-plate boundary layer. *Theoretical and Computational Fluid Dynamics* 2012;:1–19.

30. Pascal L, Piot E, Casalis G. Analyse de stabilité globale et instabilité hydrodynamique dans un conduit traité acoustiquement [Global stability analysis and hydrodynamic instability in a lined duct]. In: *CFA 2014 Poitiers*. 2014:617–623.

31. Pascal L, Piot E, Casalis G. Optimal Disturbance in a Flow Duct with a Lined Wall. *Procedia IUTAM* 2015;14:256–263.

32. Rahbari I, Scalo C. Quasi-Spectral Sparse Bi-Global Stability Analysis of Compressible Channel Flow over Complex Impedance. In: *55th AIAA Aerospace Sciences Meeting*. 2017:1879.

33. Bérenger JP. A perfectly matched layer for the absorption of electromagnetic waves. *Journal of Computational Physics* 1994;114(2):185 – 200.

34. Richards SK, Zhang X, Chen XX, Nelson PA. The evaluation of non-reflecting boundary conditions for duct acoustic computation. *Journal of Sound and Vibration* 2004;270(3):539–557.

35. Hu F. A perfectly matched layer absorbing boundary condition for linearized Euler equations with a non-uniform mean flow. *Journal of Computational Physics* 2005;208(2):469 – 492.

36. Rienstra SW. Impedance models in time domain, including the extended Helmholtz resonator model. In: *12th AIAA/CEAS Aeroacoustics Conference*. AIAA-2006-2686; 2006:1–20.

37. Hesthaven JS, Warburton T. Nodal Discontinuous Galerkin Methods Algorithms, Analysis, and Applications. 1st ed.; Springer Publishing Company, Incorporated; 2007.

38. Pascal L, Piot E, Casalis G. Discontinuous Galerkin method for the computation of acoustic modes in lined flow ducts with rigid splices. *Journal of Sound and Vibration* 2013;332(13):3270 – 3288.

39. Hernandez V, Roman JE, Vidal V. SLEPc: A Scalable and Flexible Toolkit for the Solution of Eigenvalue Problems. *ACM Trans Math Softw* 2005;31(3):351–362.

40. Geuzaine C, Remacle JF. Gmsh Reference Manual; 2013.

41. Goursaud B. Etude mathématique et numérique de guides d'ondes ouverts non uniformes, par approche modale [Mathematical and numerical study of non uniform open waveguides, modal approach]. Ph.D. thesis; Ecole Polytechnique X; 2010.

42. Kim S. Analysis of a PML method applied to computation of resonances in open systems and acoustic scattering problems. Ph.D. thesis; Texas A&M University; 2009.

43. Tumin A, Amitay M, Cohen J, De Zhou M. A normal multimode decomposition method for stability experiments. *Physics of Fluids* 1996;8(10):2777–2779.

44. Tumin A. Multimode decomposition of spatially growing perturbations in a two-dimensional boundary layer. *Physics of Fluids* 2003;15(9):2525–2540.

45. Monschke JA, Kuester MS, White EB. Acoustic receptivity measurements using modal decomposition of a modified Orr-Sommerfeld equation. *AIAA Journal* 2016;54(3):805–815.

46. Swinbanks MA. The sound field generated by a source distribution in a long duct carrying sheared flow. *Journal of Sound and Vibration* 1975;40(1):51–76.

47. Marx D. Numerical simulation of physical instabilities in a lined channel using the linearized euler equations. In: *CFA 2014 Poitiers*. 2014:583–589.

48. Pascal L, Piot E, Casalis G. A New Implementation of the Extended Helmholtz Resonator Acoustic Liner Impedance Model in Time Domain CAA. *Journal of Computational Acoustics* 2015;:1550015.

49. Monteghetti F, Matignon D, Piot E, Pascal L. Design of broadband time-domain impedance boundary conditions using the oscillatory-diffusive representation of acoustical models. *The Journal of the Acoustical Society of America* 2016;140(3):1663–1674.